CONF-750744--1

PREPRINT UCRL-76967

Lawrence Livermore Laboratory

A NUMERICAL STUDY OF ROTATING RELATIVISTIC STARS

James R. Wilson

August 25, 1975

This paper was prepared for presentation at a course on "Physics and Astrophysics of Neutron Stars and Black Holes," sponsored by the Italian Physical Society, at the Enrico Fermi Summer School of Varenna, Italy, July 14 to 26, 1975.

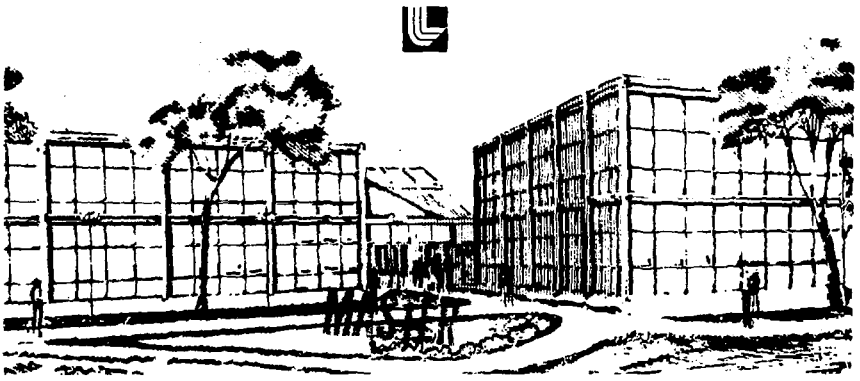

A NUMERICAL STUDY OF ROTATING RELATIVISTIC STARS*

James R. Wilson

ABSTRACT

The equations of structure for rotating stars in general relativity are presented and put in a form suitable for computer calculations. The results of equilibrium calculations for supermassive stars, neutron stars, and magnetically supported stars are reported, as are calculations of collapsing, rotating, and magnetized stars in the slowly changing gravitational field approximation.

INTRODUCTION

Rotating supermassive stars have been long considered as possible energy sources for quasars [Fowler[1]]. We first study equilibrium configurations of rotating supermassive stars to ascertain the amount of binding energy available before the stars become unstable in final collapse. The present method can describe many sorts of equilibrium stars; however, the problem of stability is still only partially understood. Axisymmetric stability can be studied by present methods for cases where heat flow and viscosity are negligible. Nonaxisymmetric instabilities are still uncertain. Stars supported by thermal pressure and massive cold stars supported by a toroidal magnetic field are studied. The interest in magnetically supported stars arises because in the collapse of a large cloud of slowly rotating gas with an initial magnetic field, the inside tends to rotate much faster and wind up the field lines into a toroidal field. Such a configuration might have a short lifetime because of magnetic braking by the rapidly rotating core and the slowly rotating envelope. It may, however, be an important intermediate

*This work was performed under the auspices of the U.S. Energy Research & Development Administration.

step in forming magnetically driven jets [see LeBlanc and Wilson (2)]. Magnetically supported stars can have very high binding energies even when the stars are nearly spherical.

We consider rapidly rotating neutron stars to see if the mass can differ from that of a nonrotating star. With a sufficiently large amount of rotation, a star of any mass can be self-supporting. The real question is how much rotation a star can have before it becomes nonaxially unstable. Applying Newtonian ideas in an intuitive manner suggests that the mass of a neutron star can only increase by about 50% from rotation without becoming unstable.

We also calculate the collapse of supermassive rotating magnetized stars with a method of calculating the gravitational fields that assumes the gravitational field is equal to the field present if the star were not collapsing. This is probably a good approximation for all the calculations presented here, because the high velocities affecting a large fraction of the star mass are either rotational about the axis of symmetry or radially inward. The quadrupole moments are slowly changing. The reason for these calculations is to see if during the collapse sufficient magnetic field is generated in the interior to form a magnetic bubble that would blow to the surface as a jet. In these calculations, both magnetic braking effects and very weak jet effects are observed. Some indication of how electrically charged black holes might be formed was found.

EQUATIONS

The gravitational field equations and metric were developed by Bardeen and Wagoner[3]. The metric is taken to be

$$(1) \qquad ds^2 = B^2 e^{2F}\left[e^{2C}\,(dR^2 + dZ^2) + R^2\,(d\phi - \omega dt)^2\right] - e^{-2F}dt^2.$$

The magnetic field is described by the toroidal magnetic field H_ϕ and by the toroidal component of the vector potential A_ϕ. These determine

completely the magnetic field due to axial symmetry. The steller material is assumed to be a perfect conductor. We express this by setting the electric field co-moving with the material equal to zero:

$$E^{o}_{\nu} = U^{\mu}F_{\mu\nu} = 0. \tag{2}$$

The electromagnetic field tensor is $F_{\mu\nu}$ and U^{μ} is the material four velocity. From this condition of perfect conductivity, the components of the electromagnetic tensor are found to be

$$\begin{cases} F_{RZ} = H_{\phi} & F_{R\phi} = \dfrac{\partial A_{\phi}}{\partial R} \qquad F_{Z\phi} = \dfrac{\partial A_{\phi}}{\partial Z} \\ F_{tZ} = V^{\phi}\dfrac{\partial A_{\phi}}{\partial Z} - V^{R}H_{\phi} & F_{tR} = V^{\phi}\dfrac{\partial A_{\phi}}{\partial R} + V^{Z}H_{\phi} \\ F_{t\phi} = -V^{R}\dfrac{\partial A_{\phi}}{\partial R} - V^{Z}\dfrac{\partial A_{\phi}}{\partial Z} \quad \text{with} \quad V^{\mu} = U^{\mu}/U^{t}\ . \end{cases} \tag{3}$$

For the gravitational field equations, we form the electromagnetic energy tensor in the locally nonrotating frame and add that energy as a source to the Bardeen-Wagoner field equations. This gives the following (G = c = 1):

$$\begin{cases} \vec{\nabla}\cdot(B\,\vec{\nabla}\,F) + \dfrac{R^2B^3}{2}e^{4F}\,\vec{\nabla}\omega\cdot\vec{\nabla}\omega = -Q_m - Q_e\ ; \\ Q_m = 4\pi B^3 e^{2F+2C}\left\{(\rho+\varepsilon+P)[2(U^t)^2-1]+2P\right\}\ ; \\ Q_e = 4\pi B\left\{\dfrac{e^{-2F-2C}}{B^2}H_{\phi}^2 + \dfrac{(1+v_{\phi}^2)e^{2F}}{R^2B^2}\left[\left(\dfrac{\partial A_{\phi}}{\partial R}\right)^2+\left(\dfrac{\partial A_{\phi}}{\partial Z}\right)^2\right]\right. \\ \qquad + \dfrac{2v_{\phi}H_{\phi}}{BR}\left(V^{R}\dfrac{\partial A_{\phi}}{\partial Z} - V^{Z}\dfrac{\partial A_{\phi}}{\partial R}\right) + \dfrac{e^{2F+2C}}{R^2B^2}\left(V^{R}\dfrac{\partial A_{\phi}}{\partial R} + V^{Z}\dfrac{\partial A_{\phi}}{\partial Z}\right)^2 \\ \qquad \left. + e^{2F}H_{\phi}^2\left[\left(V^{R}\right)^2+\left(V^{Z}\right)^2\right]\right\}\ ; \end{cases} \tag{4}$$

$$
(4)\quad
\begin{cases}
\vec{\nabla}\cdot(R^2B^3e^{4F}\,\vec{\nabla}\omega) = -P_m - P_e\ ; \\[2ex]
P_m = 16\pi RB^4 v_\phi(\rho + e + P)e^{4F+2C}\,(U^t)^2\ ; \\[2ex]
P_e = 16\pi B\left\{-H_\phi\left(V^Z\frac{\partial A_\phi}{\partial R} - V^R\frac{\partial A_\phi}{\partial Z}\right)e^{2F} + \frac{v_\phi}{BR}\left[\left(\frac{\partial A_\phi}{\partial R}\right)^2 + \left(\frac{\partial A_\phi}{\partial Z}\right)^2\right]\right\}; \\[2ex]
\vec{\nabla}\cdot(R\vec{\nabla}B) = +R_m + R_e\ ; \\[2ex]
R_m = 16\pi RB^3Pe^{2F+2C}\ ; \\[2ex]
R_e = 8\pi\ RB\left[\frac{H_\phi^2\,e^{-2F-2C}}{B^2} + \left(V^R\frac{\partial A_\phi}{\partial R} + V^Z\frac{\partial A_\phi}{\partial Z}\right)^2\frac{e^{2F+2C}}{R^2}\right]\ ; \\[2ex]
\frac{\partial C}{\partial R} = \left[\left(1 + \frac{R}{B}\frac{\partial B}{\partial R}\right)S_1 + \frac{R}{B}\frac{\partial B}{\partial Z}S_2\right]\Big/\left[\left(1 + \frac{R}{B}\frac{\partial B}{\partial R}\right)^2 + \left(\frac{R}{B}\frac{\partial B}{\partial Z}\right)^2\right]; \\[2ex]
S_1 = S_m' + S_e'\ ; \\[2ex]
S_m' = R\left\{\left(\frac{\partial\ \log\ B}{\partial Z}\right)^2 - \left(\frac{\partial\ \log\ B}{\partial R}\right)^2 - \frac{1}{2B}\left(\frac{\partial^2 B}{\partial Z^2} - \frac{\partial^2 B}{\partial R^2}\right)\right. \\
\qquad \left. + \left(\frac{\partial F}{\partial R}\right)^2 - \left(\frac{\partial F}{\partial Z}\right)^2 - \frac{R^2B^2}{4}e^{4F}\left[\left(\frac{\partial\omega}{\partial R}\right)^2 - \left(\frac{\partial\omega}{\partial Z}\right)^2\right]\right\}\ ; \\[2ex]
S_e' = 8\pi\left[\frac{v_\phi H_\phi}{B}\left(V^Z\frac{\partial A_\phi}{\partial Z} - V^R\frac{\partial A_\phi}{\partial R}\right)\right. \\
\qquad \left. - \frac{\partial A_\phi}{\partial R}\frac{\partial A_\phi}{\partial Z}(1 - v_\phi^2)\frac{e^{-2F}}{B^2R} + e^{2F}RU^tV^RH_\phi^2\right]\ ; \\[2ex]
S_2 = S_m^2 + S_e^2\ ; \\[2ex]
S_m^2 = R\left\{\frac{1}{B}\frac{\partial^2 B}{\partial R\partial Z} - \frac{2}{B^2}\frac{\partial B}{\partial R}\frac{\partial B}{\partial Z} + 2\frac{\partial F}{\partial R}\frac{\partial F}{\partial Z} - \frac{R^2B^2e^{4F}}{2}\frac{\partial\omega\partial\omega}{\partial R\partial Z}\right\}\ ; \\[2ex]
S_e^2 = 8\pi\left\{\left[\left(\frac{\partial A_\phi}{\partial Z}\right)^2 - \left(\frac{\partial A_\phi}{\partial R}\right)^2\right](1 - v_\phi^2)\frac{e^{-2F}}{RB^2} + Re^{2F}\left[\left(V^R\right)^2 - \left(V^Z\right)^2\right]H_\phi^2\right\}\ .
\end{cases}
$$

The linear rotational velocity in the locally nonrotating frame is v_ϕ, P is the material pressure, ρ is the particle density, and ϵ is the thermal energy density.

To find the equations of motion, we take the material energy momentum tensor for a perfect fluid consistent with the field equations:

$$T_{\mu\nu} = (\rho + \epsilon + P)U_\mu U_\nu + g_{\mu\nu}P \ , \tag{5}$$

which satisfies the divergence equations

$$T^{\nu}_{\mu;\nu} = \frac{1}{\sqrt{-g}} \frac{\partial}{\partial x^\nu} (T^\nu_\mu \sqrt{-g}) + \frac{1}{2} \frac{\partial g^{\alpha\beta}}{\partial x^\mu} T_{\alpha\beta} = 0 \ . \tag{6}$$

Putting this in a form suitable for computations we introduce a momentum density $S_\mu = (\rho + \epsilon + P)U_\mu U^t$, time four velocity $V^\nu = U^\nu/U^t$, and number density $D = \rho U^t$. The proper number density of the fluid is ρ, ϵ is the thermal energy density, P the pressure, and U^μ the usual four velocity. With manipulation, the energy and particle conservation equations become

$$\frac{1}{\sqrt{-g}} \frac{\partial}{\partial x\nu} (S_\mu V^\nu \sqrt{-g}) + \frac{\partial P}{\partial x\mu} + \frac{1}{2} \frac{\partial g^{\alpha\beta}}{\partial x\mu} \frac{S_\alpha S_\beta}{S^t} = 0 \ . \tag{7}$$

The particle conservation equation is

$$\frac{1}{\sqrt{-g}} \frac{\partial}{\partial x\nu} (DV^\nu \sqrt{-g}) = 0 \ . \tag{8}$$

These equations are sufficient to determine the flow. The three space-like momentum equations of eq. (7) and the time projected part of $T^\mu_{\nu;\mu}$ are used to find the time behavior of ϵ.

Consider $U^{\nu}T^{\mu}_{\nu;\mu} = 0$. Using the condition $U^{\nu}U_{\nu} + 1 = 0$ to evaluate and simplify the divergence terms, and introducing an energy density $E = \rho U^{t}$, the energy equations become

$$\frac{\partial}{\partial x^{\mu}} (EV^{\mu}\sqrt{-g}) + P \frac{\partial}{\partial x^{\mu}} (U^{t}V^{\mu}\sqrt{-g}) = 0. \tag{9}$$

We use this form to make the equations as similar as possible to the Newtonian Eulerian hydrodynamic equations, for which a large body of numerical methods exist.

To the momentum eq. (7), the electromagnetic force $f_{\mu} = J^{\nu}F_{\nu\mu}$ is added. The electric currents are given by

$$J^{R} = \frac{e^{-2C-2F}}{BR}\left\{\frac{\partial}{\partial Z}\left(BRe^{-2C-2F}H_{\phi}\right) + \frac{\partial}{\partial t}\left(RBe^{-2C}\left[\omega\left(\frac{\partial A_{\phi}}{\partial Z} + \frac{\partial A_{\phi}}{\partial R}\right) + \left(H_{\phi}V^{Z} - \frac{\partial A_{\phi}}{\partial R}V^{\phi}\right)\right]\right)\right\};$$

$$J^{Z} = \frac{e^{-2C-2F}}{BR}\left\{\frac{\partial}{\partial R}\left(BRe^{-2C-2F}H_{\phi}\right) + \frac{\partial}{\partial t}\left(e^{-2C}\left[\omega\left(\frac{\partial A_{\phi}}{\partial Z} + \frac{\partial A_{\phi}}{\partial R}\right) - \left(H_{\phi}V^{R} + \frac{\partial A_{\phi}}{\partial Z}\right)\right]\right)\right\};$$

$$J^{\phi} = \frac{e^{-2C-2F}}{BR}\left\{\frac{\partial}{\partial R}\left[\left(\omega v_{\phi} + \frac{e^{-2F}}{BR}\right)\frac{\partial A_{\phi}}{\partial R} - \omega BRe^{2F}V^{Z}H_{\phi}\right] + \frac{\partial}{\partial Z}\left[\left(\omega v_{\phi} + \frac{e^{-2F}}{BR}\right)\frac{\partial A_{\phi}}{\partial Z} + \omega BRe^{2F}V^{R}H_{\phi}\right] - \frac{\partial}{\partial t}\left[\frac{e^{2F+2C}}{RB}\frac{\partial A_{\phi}}{\partial t}\right]\right\};$$

$$J^{t} = e^{-2C-2F}\left\langle\frac{\partial}{\partial R}\left\{BRe^{2F}\left[\left(V^{\phi} - \omega\right)\frac{\partial A_{\phi}}{\partial R} - V^{Z}H_{\phi}\right]\right\} + \frac{\partial}{\partial Z}\left\{BRe^{2F}\left[\left(V^{\phi} - \omega\right)\frac{\partial A}{\partial Z} + V^{R}H_{\phi}\right]\right\}\right\rangle.$$

The time evolution of the vector potential comes from the definition of $F_{t\phi}$:

$$\frac{\partial A_\phi}{\partial t} = - V^R \frac{\partial A_\phi}{\partial R} - V^Z \frac{\partial A_\phi}{\partial Z} . \tag{10}$$

The equation for the toroidal magnetic field comes from the Maxwell equation

$$F_{\mu\nu,\eta} + F_{\eta\mu,\nu} + F_{\nu\eta,\mu} = 0.$$

With $\mu = R$, $\nu = Z$, $\eta = t$ the equation for the toroidal magnetic field is

$$\frac{\partial H_\phi}{\partial t} = \frac{\partial}{\partial Z}\left(V^\phi \frac{\partial A_\phi}{\partial R} + V^Z H_\phi\right) + \frac{\partial}{\partial R}\left(V^\phi \frac{\partial A_\phi}{\partial Z} - V^R H_\phi\right) . \tag{11}$$

To determine static configurations only, the R,Z components of the momentum equations and the gravitational field equations are needed. Since these equations are solved over a limited region of space, the boundary conditions are important. The gravitational potentials are estimated to order $1/r^3$ as follows:

$$\begin{cases} F = M\left(1 - \frac{r}{6}\frac{\partial B}{\partial r}\right)\Big/ r + Q(2Z^2 - R^2)/r^5 \\ B = 1 - \frac{2}{r}\frac{\partial B}{\partial r} \\ \omega = 2J/r^3 \qquad r^2 = R^2 + Z^2 \\ C = 0 \quad \text{on axis.} \end{cases} \tag{12}$$

The gravitational mass M is given by

$$M = 2\pi \int \left(T_R^R + T_Z^Z + T_\phi^\phi - T_t^t\right) dRdZ\sqrt{-g} = M_m + M_{\text{[illegible]}} ;$$

$$M_m = 2\pi \int \left[(\rho + \varepsilon + 3P) + \left(S_R V^R + S_Z V^Z + S_\phi V^\phi\right)\right] dRdZ\sqrt{-g} ;$$

$$M_{\ell} = 2\pi \int \left\{ \frac{H_{\phi}^{\,2}}{B^2} \left[\frac{e^{-4F-4C}}{B^2} + e^{-2C} \left((V^R)^2 + (V^Z)^2 \right) \right] \right.$$

$$+ \left(\frac{\partial A_{\phi}}{\partial R} \right)^2 + \left(\frac{\partial A_{\phi}}{\partial Z} \right)^2 \frac{e^{-2C}}{R^2 B^2} \left[1 + RBv_{\phi} e^{2F} \left(V^{\phi} + \omega \right) \right]$$

$$+ \frac{H_{\phi} V^{\phi}}{B} e^{-2C} \left(V^R \frac{\partial A_{\phi}}{\partial Z} - V^Z \frac{\partial A_{\phi}}{\partial R} \right)$$

$$\left. + \frac{1}{R^2 B^2} \left(V^R \frac{\partial A_{\phi}}{\partial R} + V^Z \frac{\partial A_{\phi}}{\partial Z} \right)^2 \right\} dRdZ\sqrt{-g} .$$

The angular momentum J is written as the sum of

$$J_m = 2\pi \int S_{\phi} \sqrt{-g}\, dRdZ ;$$

$$J_{\ell} = 2\pi \int \frac{e^{-2C}}{B^2} \left\{ H_{\phi} \left(\frac{\partial A_{\phi}}{\partial Z} V^R - \frac{\partial A_{\phi}}{\partial R} V^Z \right) \right.$$

$$\left. + (V^{\phi} - \omega) \left[\left(\frac{\partial A_{\phi}}{\partial R} \right)^2 + \left(\frac{\partial A_{\phi}}{\partial Z} \right)^2 \right] \right\} \sqrt{-g}\, (dRdZ) .$$

The quadrupole moment Q is approximated by integrating the mass contributions multiplied by $(2Z^2 - R^2)$;

$$Q = 2\pi \int \left(T_R^{\,R} + T_Z^{\,Z} + T_{\phi}^{\,\phi} - T_t^{\,t} \right) \left(2Z^2 - R^2 \right) \sqrt{-g}\, (dRdZ) .$$

The differential equation for B is linear in B, so that it does not have a source as seen from far away. Its asymptotic form arises from the R factor of the differential term $\vec{\nabla} \cdot (R\vec{\nabla}B)$ in the equation for B.

The term $\frac{M}{6} \frac{\partial B}{\partial r}$ in the asymptotic form of F arises from the B term in the differential equation for F; $\vec{\nabla} \cdot (B\vec{\nabla}F)$.

The equation for C is an ordinary differential equation and C = 0 on the axis; it is sufficient to integrate C out in R from the axis.

The magnetic field variable A_{ϕ} is taken as zero at the outside of the calculational grid and H_{ϕ} is taken as zero outside the region occupied by

material. It may seem artificial to set A_ϕ equal to zero on the boundary of the calculational grid; however, with $A_\phi = 0$ at the boundary, there is no external torque and the system as a whole is electrically neutral. In practice, the force needed at the boundary to constrain the magnetic field to the interior regions is extremely small.

METHOD OF SOLUTION

First, we discuss the manner of solution for stationary equilibrium calculations. In this case, besides the gravitational field equation, it is necessary to solve only the two momentum equations for hydrostatic equilibrium

$$(13)\begin{cases} \dfrac{\partial P}{\partial R} + \dfrac{1}{2}\dfrac{\partial g^{\alpha\beta}}{\partial R} U_\alpha U_\beta (\rho + \varepsilon + P) + J^\alpha F_{\alpha R} = 0, \\ \text{and} \qquad\qquad \alpha,\beta = \phi, t \\ \dfrac{\partial P}{\partial Z} + \dfrac{1}{2}\dfrac{\partial g^{\alpha\beta}}{\partial Z} U_\alpha U_\beta (\rho + \varepsilon + P) + J^\alpha F_{\alpha Z} = 0. \end{cases}$$

Space is divided by a rectangular grid in R and Z, and the variables are centered as in Fig. 1. Difference equations are found from the differential equations by taking appropriate first order differences with Fig. 1 as a guide. All equations are centered at the same space point by suitable averages. A density distribution in R,Z space is chosen for equilibrium calculations. If the star is nonmagnetic, then the velocities, energy and pressure are taken to be zero on the first iteration and the field equations (eq. 4) are solved with only the density source terms. The Z component of eq. (13) is solved for P, and hence ε. An appropriate equation of state both relates P, ε, and ρ. The R component of eq. (13) is then solved for both the angular momentum U_ϕ with the P and ε just found, and the velocity normalization condition $U^\alpha U_\alpha + 1 = 0$. The new ρ, ε, P, S_ϕ are now put into the source terms of eq. (4).

These equations are solved for new values of the gravitational potentials. The equations for gravitational potentials involve several potentials. To separate the unknowns the following procedure is used. In the differential form for example, $\vec{\nabla} \cdot (B\vec{\nabla}F)$ in the first of eq. (4) B has its value from the last iteration and all other variables use old values. Source-like terms use the old F. The resulting simple difference equation is solved for F. The next equation is solved for ω by a similar method. Terms on the left side use old values (except ω) and all terms on the right side use old values, including the old values for ω. After new values of the potentials are found, the equilibrium eqs. (13) are solved again for new values of P, ρ, and S_r. This process is repeated until convergence is achieved. Calculations are only made for magnetic stars with toroidal fields. In this case, the ρ and P are zero and the Z component of eqs. (13) is solved for H_ϕ instead of ρ. The rest of the solution is identical to that of thermally supported stars.

With dynamic calculations we assume that for any moment the gravitational field is the field that would have existed had the sources been constant. For any moment, the source terms are evaluated with the density, energy, velocity, and fields at that moment. The meaning of this approximation is not clear for very strong gravitational fields. As a check on the emitted gravitational radiation, the energy

$$E = \frac{1}{M}\int (\ddot{Q})^2 dt$$

is calculated, and in all calculations performed, this is a very small quantity ($\lesssim 10^{-6}$).

After finding the gravitational field potentials, we solve the fluid and magnetic field equations by standard finite difference methods using finite time steps and a finite space grid. The system is advanced from one time to

the next by solving the time evolution equations for the material variables and the magnetic fields, and again solving the gravitational field equations. The calculational grid is also moved in time so that at any moment it spans the stellar material in a reasonable fashion. For example, in collapse calculations, the grid is moved inward so that the amount of material in the central zones of the grid changes as little as possible. To keep the zoning reasonably good, the outside of the grid is moved in and some mass is lost. The lost mass is of very low density and presumed to be unimportant.

RESULTS FOR EQUILIBRIUM CONFIGURATIONS

We first discuss thermally and rotationally supported stars with a perfect gas equation of state. The adiabatic index is 4/3, which is appropriate to a supermassive star [Fowler[1]]. A density profile is selected according to the formula

$$(14)\quad \begin{cases} D = D_o\,(1 + aY + bY^2)\exp(-Y) \\ Y = (R^n + (\alpha Z)^n)^{1/n}\ . \end{cases}$$

The parameters a,b make the central density either peaked or flat. The principal parameter α determines the overall shape; n makes the distribution either elliptical or more square as projected on the R,Z plane. The initial density is chosen so that the star will be almost Newtonian and an equilibrium solution for the thermal energy and rotational velocity is easily found. After one solution is found, D is multiplied by a constant a little greater than one and a new solution is found for the higher mass. This process is repeated until the binding energy is past its maximum value. This way, a sequence of stars with the same shape and increasingly large gravitational fields is generated. The parameter for the gravitational field strength is

$\gamma = 1 - \exp(-F_c)$, where F_c is the central value of the potential F, and γ is related to the central red shift by $\gamma = Z_c/(1 + Z_c)$.

We first give the results for an elliptical (n = 2) density distribution with a = 0, b = 0. In Fig. 2 the binding energy (particle mass - gravitational mass)/(particle mass) for a variety of shapes, α, is presented. The disk ($\alpha = \infty$) calculation is from Bardeen and Wagoner [3]. Figure 3 shows the specific angular momenta of the several configurations as a function of γ. It is interesting to conjecture about the change in the binding energy curves with α. For $\alpha > 6$ the shapes are characteristic of disk stars and appear to have no maximum below $\gamma = 1$. Also, the high-α stars appear to have a specific angular momentum that approaches the extreme Kerr solution for $\gamma = 1$. Highly flattened stars are qualitatively related to extreme Kerr metrics, while round stars can not be continuously connected to the Kerr metric.

All these stars rotate more rapidly at the center than at the outside. Uniform rotation limits the amount of binding energy to considerably lower values. Figure 4 shows how the angular velocity falls off with R and Z for an $\alpha = 8$ star with a $\gamma = 0.5$. The gradient of the angular velocity is very small in the Z direction. For high values of α and γ an ergo-toroid develops inside the star; i.e., a surface where $g_{tt} = 0$. In Fig. 5 the linear frame dragging velocity [V = WBRexp(2F)] is shown as a function of R for several values of γ. The boundary of the ergo-toroid region is V = 1. In Fig. 6 the shapes of the ergo-toroid regions are shown for several values of γ. Such regions can extend far outside the star. Figure 7 illustrates how space is being stretched. As mass is initially added to the grid, the density increases with γ, but eventually space begins to sag as more matter is added and the density decreases. Finally, in Fig. 8 the variation of several quantities with shape are shown. The ratio of kinetic to potential energy is

important since Ostriker and Tassoul[4] have shown for Newtonian stars that KE/GE < 0.14 for secular stability and KE/GE < 0.27 for dynamic instability. The former condition restricts the shape of stars to $\alpha \leq 2$ and the latter condition restricts to $\alpha \leq 3$. Thus, very relativistic stars are probably unstable to nonaxisymmetric deformations. The equation of state adiabatic index is 4/3, implying that these stars have small binding energies.

The thermal energy density curve is used to estimate where local instability might occur; i.e., a Jeans' type gravitational instability. As stars move away from disk configuration ε rises very rapidly, so only very flat stars are unstable in local breakup. These flat stars presumably could not form except in a very short time because the bar-type instability sets in at $\alpha = 3$ and develops rapidly in a few revolutions. Three-dimensional Newtonian hydrodynamic calculations were made to confirm Ostriker and Tassoul's[4] stability criteria because their stability analyses uses a moderately restrictive class of trial functions [see Appendix]. It is not obvious how strong differential rotation might affect their results. Our computer calculations agree roughly with the onset of a dynamic instability at $\alpha \overset{\sim}{=} 3$ and KE/GE $\overset{\sim}{\sim} 0.28$ [for stars with the same differential rotation distribution as relativistic equilibrium stars]. By "dynamic" we mean the star changes shape dramatically. Stars with 0.14 < KE/GE < 0.25 change shape very slowly and the distortions are not apparent by visual inspection of iso-density curves, but can be detected by quadrupole moment edits.

Three equilibrium configurations were tested for axial stability on the dynamic computer program. Stars with α = 2, 4, and 8, and with γ's of 0.089, 0.407, and 0.82, respectively, were run. They were run for times corresponding to 20 to 40 sound-transit times across the star. The equilibrium and dynamic difference equations are centered differently in space so they are

not equivalent. The stars jiggle about, but the overall shape and mean density change very little. We conclude that at least all models with $d(BE)/d\gamma$ greater than zero are stable to axially symmetric perturbations.

The parameters a, b, and n are varied for a few configurations to see how sensitive the general results are to details of the density. Binding energy is very insensitive to a, b, and n at the same value of γ. The curves of constant angular velocity could be parallel (in R,Z space) to the rotation axis and the entropy could always increase outward by adjustments of $a < 1$, $b < 1$, $2 \leq n \leq 4$. Local instabilities such as the Taylor and Goldrich[5] instabilities can thus be avoided.

Because roundish stars cannot become highly relativistic, and flat stars are unstable toward breakup, a rapidly rotating black hole cannot be formed by a sequence of equilibrium states. It must be formed by dynamic collapse. This result is clear for supermassive stars with an adiabatic index of 4/3. Calculations were also performed with an adiabatic index of 2, which might be representative of very stiff hot neutron star matter. In this case, $\alpha = 4$ behaves like a disk and $\alpha = 2$ is like a round star [see Wilson[6]].

The next type of rotating star we consider is the cold neutron star. Thermal energy is not a free parameter in this case, so a different solution must be used. First, a guess of the density distribution for a spherical neutron star is put in the grid and the field equations are solved for the gravitational potentials. Then the Z equation for equilibrium (eq. 13) is integrated out from the equatorial plane to find the density profile in equilibrium with the gravitational fields. The density D is fixed on the equator. The the R equation is solved for the equilibrium angular velocity. This process is repeated until a convergence is obtained. This procedure describes an almost spherical neutron star, depending on how well the initial

density is guessed. Next, the density profile is stretched uniformly by a small amount in the R direction and the whole iteration process is repeated until an equilibrium is achieved. This develops a sequence of faster and faster rotating stars with about the same central densities. The central proper density changes along a calculational sequence because the coordinate density D is maintained on the equator.

We use an equation of state with a maximum stable spherical mass of 1.9 $M_\odot$. In Fig. 9 the masses and central densities of rotating stars in sequence are shown. Figure 10 shows the mass increase from rotation vs stellar shape. Comparing Newtonian star shapes with their kinetic energy to gravitational potential energy ratio, we estimate that the critical ratio 0.14 for kinetic energy to gravitational energy corresponds to a shape ratio of $R/Z \approx 1.75$. The increase is fairly independent of central density (Fig. 10). Also in Fig. 10 is the curve for an extreme equation of state having a maximum spherical mass of 3.3 $M_\odot$. We infer the rotational mass increase to be moderately independent of the equation of state, and the maximum stable rotational enhancement to be 1.5 to 1.7. The isodensity contours of these models are elliptical near the center and oval toward the outside. Angular velocity is nearly constant on lines of equal cylindrical coordinate radius, but the stars rotate differentially in the R direction. The angular velocity falls by a factor of two from the axis to the outside at the equator [see Wilson[7]].

We consider next the class of rotationally and magnetically supported stars. As stated earlier, these magnetic stars might be an intermediate step in the dynamic collapse of a rotating magnetized cloud of gas. The question is how well might the combination of rotation and magnetic field stave off collapse under relativistic conditions. We look only at toroidal

magnetic fields because these are the simplest fields and perhaps the most likely fields formed in the rapid collapse of a rotating magnetic star.

We study only the extreme case of zero material to reduce the number of parameters. The solution is similar to that for thermally supported stars. A guess of the density is made. The Z component of the equilibrium equation (eq. 13) is solved for the toroidal field component H_ϕ. The R component of the equilibrium equation is solved for the angular momentum U_ϕ. The field equations are solved as before. The density formula used for spherical stars is used again. For a spherical star, $\rho U_\phi^2 = H_\phi^2$ in the Newtonian limit. This combination of U_ϕ and H_ϕ acts somewhat like a perfect gas with an adiabatic index of 1.5.

In Figs. 11 and 12, binding energy and angular momentum dependence on the relativity parameter γ are summarized for a variety of shapes. Because of the effectively stiff equation of state, stars of the same shape have much larger binding energies than the thermally supported stars with adiabatic indexes of 4/3. A spherical star has a binding energy of 1.25%. The transition from round-type stars to disk-type stars appears to take place at $\alpha = 3$ to 4, instead of 6 to 8 as seen for stars with adiabatic indexes of 4/3. The angular momenta again converge to 1 for $\alpha > 2$. (Again, these stars have no scale, so, as for thermally supported stars, the stellar mass is taken as one.) Much rounder stars form ergo-toroids. An $\alpha = 3$ configuration just barely forms an ergo-toroid at its maximum binding energy. Figure 13 shows the curves of constant frame dragging velocity. The $V = 1$ curve is the surface of the ergo-toroid.

The stability of magnetically supported stars is less understood than that of thermally supported stars. Two of these stars ($\alpha = 1, 2$) were tested

for axially symmetric stability and were found to be stable at the configurations of peak binding energy.

Trehan and Singh[8] studied the nonaxial stability of rotating magnetized stars. They conclude that uniformly rotating stars with uniform densities should have the same ratio of gravitational potential to kinetic energy as nonmagnetic stars. The magnetic stars calculated above have a ratio of kinetic energy to potential energy that varies from 0.33 to 0.38 in the sequence $R/Z = 1$ to $R/Z = 4$. From this, we infer that these magnetic stars are unstable. However, it may not be safe to apply Trehan and Singh's criteria to these magnetic stars because the velocity distribution is extremely differential. The linear rotational velocity over the star is very flat. It rises by a factor of two going from the axis to the outside. A large fraction of the mass has essentially the same linear velocity, rather than angular velocity. This point needs further study.

RESULTS OF DYNAMIC CALCULATIONS

The dynamic calculations followed from LeBlanc and Wilson's[2] results for the collapse of a rotating magnetic iron core in a star at the end of its thermonuclear evolution. They found that an iron star collapses rapidly when iron decomposes into neutrons, producing a nonuniform angular velocity distribution because the interior collapses much faster than the outer parts. This differential rotation twists the (initially assumed) poloidal field into a very strong toroidal field. The region of strong toroidal field acquires buoyancy, rises along the axis, and forms two jets in opposite directions along the axis. The jets have a kinetic energy considerably higher than escape velocity. No such jets are seen in supernovae explosions, however they are common in radio galaxies and quasars. John Wheeler[9] points out that a supermassive star might undergo a similar collapse and form a jet. In this

case, the initial cause of collapse is the relativistic instability arising in massive stars when the increased gravitational forces of relativity increase beyond the excess of the adiabatic coefficient above 4/3. It is conjectured that the star would cool slowly and contract to the point of relativistic instability would then be supported less and less, and finally begin a very rapid infall. After a long infall, the effects of an initially negligible angular momentum and magnetic field would be felt. The star would produce a very large toroidal magnetic field and the collapse would also be halted by the increasing centrifugal effects of rotation. The twisitng of the field lines might blow a magnetic bubble out. Several configurations were tried. No jets, or only very weak jets, were formed.

The first calculation starts with a spherical density distribution that falls off exponentially with an increase in radius. Central density is taken as 5×10^{-6}. The material is given an angular velocity that is a function of cylindrical radius only which falls exponentially with the radius, and which has an exponent coefficient one-third of that used for the density distribution. The angular velocity is then normalized so that the total angular momentum is 1.5. A poloidal magnetic field generated by a current proportional to the density is also included. The full calculations are performed over an inner region where the star is considered to reside. An outer grid twice the linear size of the inner region is used to calculate the gravitational and magnetic fields. It is used to minimize the effect of the boundary conditions on the fields. No magnetic field lines leave the outer grid. This condition puts a small current on the outer boundary. The magnetic field energy is normalized to 1/70 of the gravitational energy. The rotational energy is about 1/10 of the gravitational potential energy.

The internal energy is then adjusted to where the star is slightly under-supported. In Fig. 14, several quantities integrated over the star are given as functions of time. Energies were calculated as if the quantities were Newtonian, and are to be considered only as qualitative indicators of the energy redistribution during the course of the calculations. The kinetic energy of infall KE_{RZ} rises to a maximum at a time of 1100. At the same time, the central density rises to 2.5×10^{-4}. The inside is rotating much faster than the outside. The inside slows its collapse, as seen from the decrease of KE_{RZ}. Large differential rotation strongly amplifies the toroidal magnetic field between times of 1200 and 1600. The interior rotation is slowed sufficiently to where central collapse is resumed. The calculation was terminated at a time of 1700 because the central zoning became poor. The central red shift and density at the end are 1.0 and 0.15, respectively. Collapse is assumed to be inevitable. For inner regions moving in rapidly, the specific angular momentum J/M^2 is less than one so rotation probably cannot halt the infall. Figure 15 shows the final configuration of the star's central regions. Poloidal field lines in the central region are nearly parallel to the lines of constant angular velocity. The generation of toroidal field is low in the very central regions. The electric charge plotted in Fig. 14 is the integral of all positive charges over the star: net charge is zero. The positive charge is concentrated near the center of the star, in a complex manner. The charge varies greatly from zone to zone, but in general it is positive near the center along the axis and the equator and negative toward the outside. To smooth out the fluctuations, the charge was integrated over spherical shells. The resulting average charge as a function of spherical radius is shown in Fig. 16. The integral of the charge in Fig. 16 is, to a radius of 3, about one-eighth the positive charge of Fig. 14.

The charge in Fig. 14 is thus not a good indicator of charge on the high density region. The charge appears to approach a constant value as the star collapses. From this we infer that the black hole will be formed with a significant charge.

We discuss next the only calculation giving a jet. The various energies as functions of time are plotted in Fig. 17. The initial configuration is similar to that of the previous calculation, except the initial energies were selected differently, as seen by comparing Figs. 14 and 17. In the second calculation the magnetic energy rises much more, relative to the other energies. At the time of peak magnetic energy a jet begins to form on the axis. Figure 18 shows the stellar configuration at a time 30 after peak magnetic energy when the jet reaches the outside. The contours of H_φ bluge slightly near the axis. In the jet, the ratio of magnetic energy density to mass density varies from 0.010 at Z = 15 to 0.13 at Z = 25. The material in the jet barely has escape energy. In the regions without arrows, the material generally moves outward at considerably lower velocities because the whole star is bouncing.

Several combinations of initial energy ratios were tried, but no other jets of this type formed. However, a jet is formed by another mechanism. As the star collapses, material slides down the field lines and the ratio of magnetic energy to mass density rises an order of magnitude or more in the outer regions. Late in the calculation, the Alfven velocity in the outer regions is typically 0.1. The field lines are whipped about by the collapse, giving rise to material velocities of about 0.1. When this high velocity material happens to converge onto the axis it forms a Monroe-type jet. The amount of jet material is small (less than 10^{-6}). The outside of the calculational grid is moved in, usually by a factor of 2 to 4, to maintain

good central zoning, and so the action in the outer regions is not well represented.

In addition, energy-vs-time plots of three other calculations are included. In Fig. 19, the initial exponential configuration of the first model is used, except that the ratio of magnetic field energy to gravitational field energy is 1:50, and the ratio of rotational energy to potential energy is 1:5. The R,Z kinetic energy rises to 0.001 as before, then falls and peaks before a final rise which seems to lead to collapse. The mass in the calculation is shown in Fig. 19. The indicated mass loss is the largest of any calculation, but the star had a relatively large initial angular momentum. The mass fell to about 0.9 at the end of all other calculations. In all calculations the specific angular momentum J/M^2 fell to between 0.93 and 0.97, even though the calculations started out with specific angular momenta of 1.2 to 2.0. The material leaving the grid seems to take out just enough angular momentum and, with the lost mass, leaves a star with specific angular momentum a little less than one, and thus unsupportable. The next two calculations were performed with a relatively flat central density distribution. The parameters a and b of eq. 14 were taken as 1, and the configuration was spherical as in the previous calculations. The flatter density distribution allowed the calculation to proceed further with good central zoning. The calculations were carried to a central red shift of 2. The energy summary plots are given in Figs. 20 and 21. A large change in magnetic energy produced no effect on the late time behavior. The calculation with the smaller initial magnetic field ended with the most magnetic field and both calculations ended with specific angular momenta of 0.95. These last three models have a roughly elliptical shape with a 2:1 aspect at the end of the calculations.

The initial configuration of these last two calculations and isodensity and poloidal field lines are shown in Fig. 22. The stellar configuration at a time of 510 is shown in Fig. 23. Typical poloidal field lines are smooth in the region of appreciable density but are rather distorted in the low density region. This picture is common for most calculations near the end of collapse.

All the above calculations had an angular velocity that fell off with cylindrical radius by about a factor of three from inside to outside. Two calculations were also made for initially rigid rotating stars. The inside fell in rapidly and resulted in very centrally condensed stars with much less field generation and rotation effect than the differentially rotating models.

A somewhat random selection of initial stellar configurations has been studied. A jet was formed in one calculation, but it does not commonly appear in the calculations. To explain radio jets, a frequently occuring mechanism is needed — not just a mechanism that works for a limited range of parameters of a particular model, because the jets are so common. The next step is to construct stellar models that include nuclear burning. If the burn rate is considerably greater than the Eddington radiation limit, something must give way. An explosion results when the burn rate becomes much faster than the Eddington luminosity in spherical models. The question is whether or not some combination of rotation and magnetic fields can permit either an axial explosion or burning without a general explosion in a star that is round enough to be somewhat stable.

The star with $R/Z = 3$ acquired the distortion shown in Fig. 24, where the projected area density in the plane perpendicular to the rotation axis is shown. The distortion appears and partially disappears with time, as the system rotates with the shear of non-uniform rotation. The angular velocity in the center is about twice the angular velocity at the outside. The quadrupole moment (of deformation) is about 2×10^{-3}, and again the quadrupole moment oscillates, with an amplitude of 50% for this example. The star with $R/Z = 4$ exhibited very large and immediate distortion, as expected for a star with a ratio of kinetic energy to potential energy well above the value for dynamic instability onset. The pattern shown in Fig. 25 remained similar in time as the star rotated. The material is strongly differentially rotating, but material is going in and out of the wings of the star in such a manner as to preserve the same appearance of the wings.

APPENDIX

NONAXISYMMETRIC INSTABILITIES

The star equilibrium configurations used to represent super-massive stars (with an adiabatic index of 4/3) are differentially rotating. Some doubt exists as to whether or not this differential rotation suppresses the nonaxial instabilities found for stars with uniform rotation. Equilibrium configurations with the same type of density profile were introduced into a three-dimensional Newtonian hydrodynamic computer program to study this instability. The stars were then observed for a few revolutions, in which time they appeared to find new steady states if formerly unstable. Stars with elliptical density profiles in the R,Z plane were calculated with $R/Z = 2,3,4$, which had kinetic to potential energy ratios of 1.5, 2.7, and 3.2, respectively. The star with $R/Z = 2$ did develop a quadrupole moment perpendicular to the axis corresponding to a nonaxial deformation of about 2×10^{-4} (the mass of the stars is one unit, and the central density is 10 units, so the mean stellar radius is about one).

The quadrupole moment component corresponding to nonaxisymmetric deformation rose rapidly to about 2×10^{-4} in about one revolution, and continued to rise and fall by about 0.5×10^{-4} around the value of 2×10^{-4}. The numerical methods for solving hydrodynamics have lots of dissipation built in, because of the transport of material from one zone to the next. These stars are not initially in equilibrium because the spatial-centering of the difference equations is different for determining the initial configuration and the dynamic calculations. Thus, the stars have small oscillations in the direction perpendicular to the axis, apart from the motions of instability. The concomitant dissipation should allow the star to go to other configurations of slightly different energy.

REFERENCES

1. Fowler, W. A., High Energy Astrophysics and Proceedings of Course 35 of International School of Physics "Enrico Fermi," L. Grafton Ed. (New York; Academic Press, 1965).
2. LeBlanc, J. M. and Wilson, J. R., Astrophys. J., 161, 541, 1970.
3. Bardeen, J. M. and Wagoner, R. V., Astrophys. J., 167, 359, 1971.
4. Ostriker, J. P. and Tassoul, J. L., Astrophys. J., 155, 987, 1969.
5. Goldreich, P. and Schubert, G., Astrophys. J., 150, 571, 1967.
6. Wilson, J. R., Astrophys. J., 176, 195, 1972.
7. Wilson, J. R., Phys. Rev. Lett., 30, 1082, 1973.
8. Trehan, S. K. and Singh, M., Astrophys. Space Sci., 33, 43, 1975.
9. Wheeler, J., Princeton University, private communication.

FIGURE CAPTIONS

Figure No.

1. Conceptual space grid for forming difference equations. The quantities near the vertices are centered at the vertices. The quantities in the center of zones are centered there. The equation for any quantity is centered at that quantity's position and all other quantities or differences are averaged to center at the same position.

2. The binding energy in percent of the particle mass for several shapes of stars versus the relativity parameter, γ. The other density parameters are: $a = 0$, $b = 0$, $n = 2$.

3. The specific angular momentum J/M^2 vs relativity parameter γ for several shapes of stars. The other density parameters are: $a = 0$, $b = 0$, $n = 2$.

4. The horizo tal lines are the angular velocity at cylindrical radii of 0.7 and 1.6 vs αZ ($\alpha = 8$). The angular velocity in the equator versus radius is shown by the indicated curve. The density vs either R or αZ, is ρ.

5. Frame dragging velocity vs radius in the equatorial plane of an $\alpha = 6$ star for several values of the relativity parameter γ.

6. Surfaces of $g_{tt} = 0$ are indicated in solid lines for an $\alpha = 6$ star for three values of the relativity parameter γ. The dashed curve is the surface where the density is 0.18 times the central density.

7. Proper central particle density as a function of γ for a sequence of stars with $\alpha = 6$.

8. The mean thermal energy $\bar{\epsilon}$, the ratio of kinetic to potential energy KE/GE, and the maximum binding energy vs the inverse of the shape parameter α.

9. Solid curves give the gravitational mass in solar masses for three different central density tracks vs the specific angular momentum. The dashed lines give the central densities to be associated with the mass curves: the higher the density, the higher the mass.

10. The mass of rotating neutron stars relative to spherical stars with the same central density vs the shape of the star. The quantity R/Z is found by a crude average of several isodensity lines in the R,Z plane. The dashed curve is for an equation of state that has an extremely hard equation of state. Other curves are labeled with the central density of the spherical model in the sequence.

11. Binding energy as a percent of the particle mass for shapes of magnetically supported stars and for values of the shape factor α vs the relativity parameter γ.

12. The specific angular momentum J/M^2 of magnetically supported stars for several values of the shape parameter α vs the relativity parameter γ.

13. The dashed curves are the contours of equal inertial frame velocity ($R\beta\omega e^{2F}$) in the RZ plane. The solid curve in that family is for frame velocity 1. The other curve values differ by 0.2. The solid curve that extends down to the axis is the contour for the density D, one-tenth the central density. The relativity parameter γ is 0.65. The shape factor α is 4; however, the density has been distorted some by relativistic effects.

14. The internal thermal energy IE, the kinetic energy associated with the ϕ velocity KE_{ϕ}, the kinetic energy associated with velocities in the RZ directions KE_{RZ}, the magnetic energy of the toroidal magnetic field ME_{ϕ}, the magnetic energy of the poloidal magnetic field ME_{RZ}, and the integral of the positive charge density over the volume of the star displayed as functions of time. Only small changes in the various quantities have occurred before the time of 400.

15. Isodensity surfaces are indicated by the solid lines and poloidal field lines are indicated by the dashed lines for the star of Fig. 14 at a time of 1750, the end of the calculation.

16. The charge density and mass density averaged over spherical surfaces plotted vs spherical radius r.

17. Summary of various energies vs time for the calculation that produced a jet (shown in Fig. 18). See Fig. 14 for labels.

18. Stellar configuration of a star just after an axial jet has formed. The arrows indicate RZ velocities in the R,Z plane. The longest vector represents a velocity of 0.25. The closely nested curves are isodensity curves. The dashed lines are isotoroidal magnetic field contours. The poloidal magnetic field lines start on the equator and go up and out.

19. See Fig. 14 for labels. The gravitational energy GE, instead of internal energy is plotted. The internal energy is always little less than the gravitational energy in all the calculations. Note change in time scale at 1400. The mass m remaining in the calculational grid is also plotted vs time.

20. Energies vs time. See Fig. 19 for labels. Note changes of time scale at a time of 500.

21. Energies vs time. See Fig. 19 for labels. Note change of time scale at a time of 500.

22. Idosensity contours and poloidal magnetic field lines for the calculation of Fig. 21 at zero time. The densities of the contours differ by a factor of 2.5. The central density is 1.2×10^{-5}.

23. Isodensity contours for the calculation represented in Fig. 19 at a time of 515. Included are the isototoidal magnetic field intensity contours (shown by the dashed curves) and the poloidal magnetic field lines. The densities change by a factor of 1.6 from curve to curve. The central density is 0.006. The toroidal field differs by a factor 2.4 curve to curve. Peak value is 0.013.

24. Contours of equal mass per unit area projected onto the R,ϕ plane for a rotating star that initially had a 3:1 elliptical density profile as projected in the R,Z plane.

25. Contours of equal mass per unit area projected onto the R,ϕ plane for a rotating star that initially had a 4:1 elliptical density profile as projected in the R,Z plane.

TAL/grw

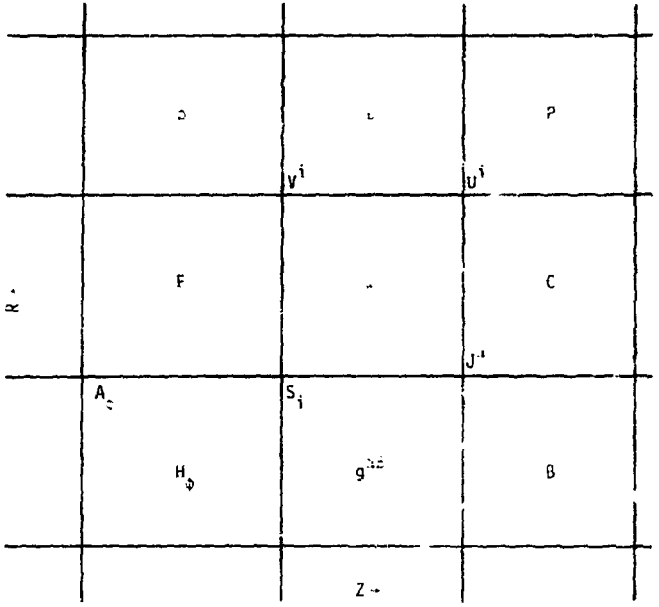

Wilson - Fig. 1

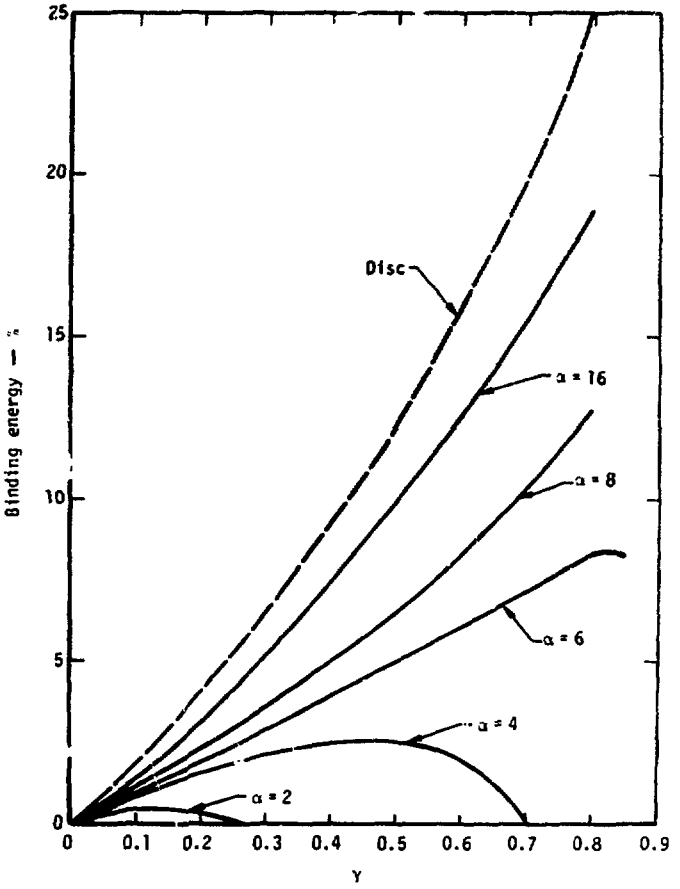
25
20
15
10
5
0
Binding energy — %
Disc
α = 16
α = 8
α = 6
α = 4
α = 2
0
0.1
0.2
0.3
0.4
0.5
0.6
0.7
0.8
0.9
Y

Wilson - Fig. 2

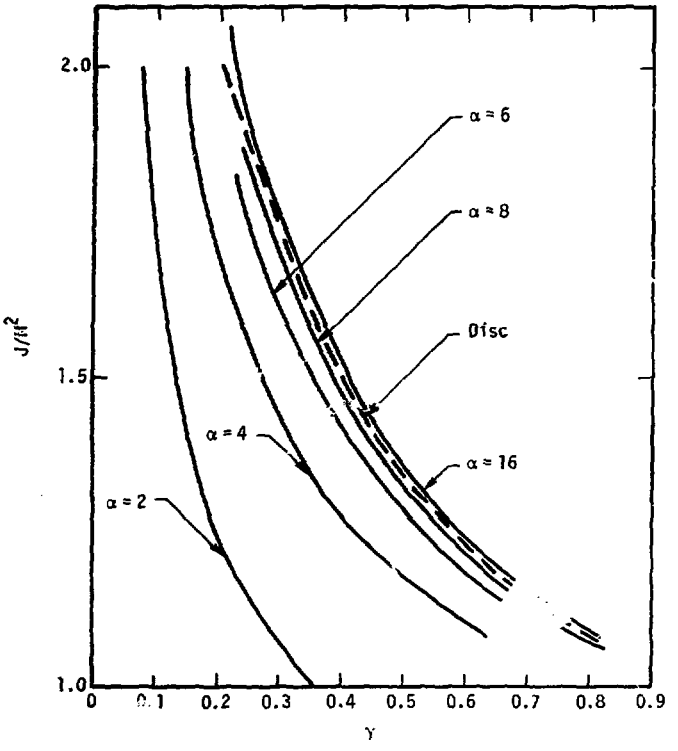

Wilson - Fig. 3

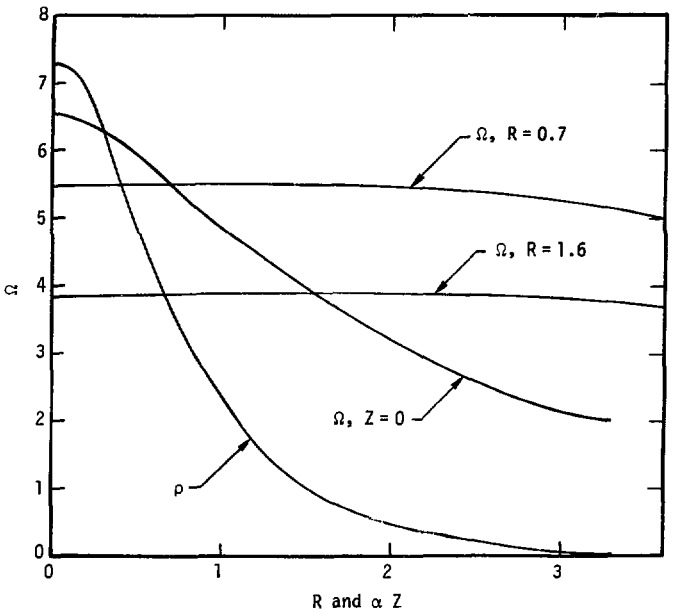

Wilson - Fig. 4

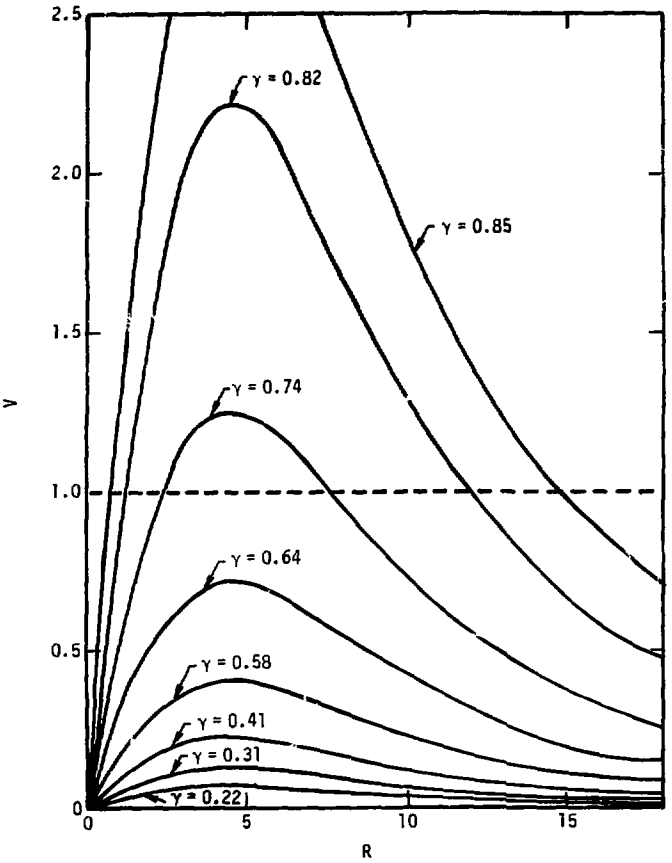
2.5
2.0
1.5
1.0
0.5
0
V
0
5
10
15
R
γ = 0.82
γ = 0.85
γ = 0.74
γ = 0.64
γ = 0.58
γ = 0.41
γ = 0.31
γ = 0.221

Wilson - Fig. 5

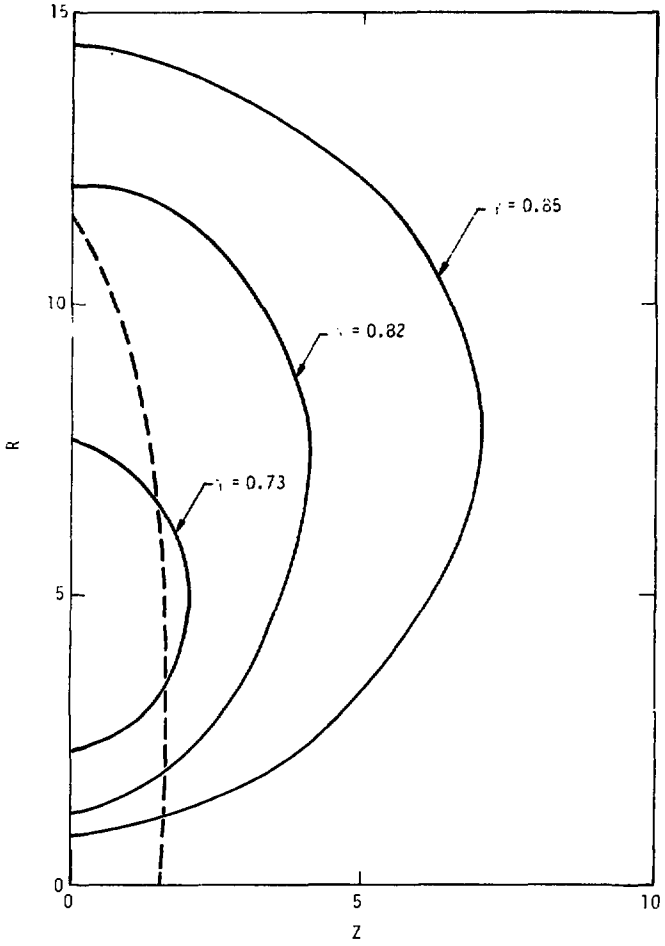

Wilson - Fig. 6

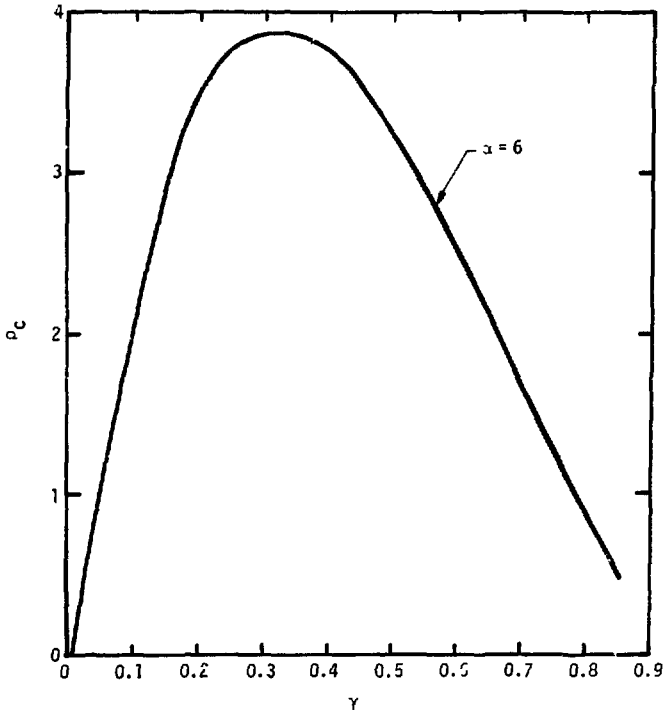

Wilson - Fig. 7

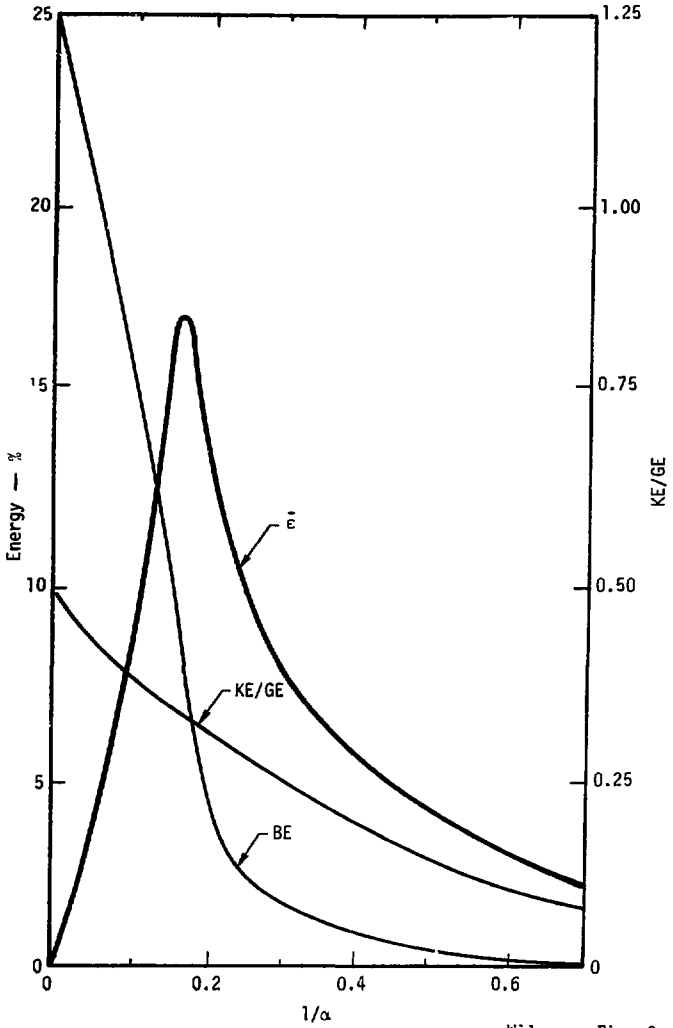
25
20
15
10
5
0
1.25
1.00
0.75
0.50
0.25
0
0
0.2
0.4
0.6
1/α
Energy — %
KE/GE
ε'
KE/GE
BE

Wilson - Fig. 8

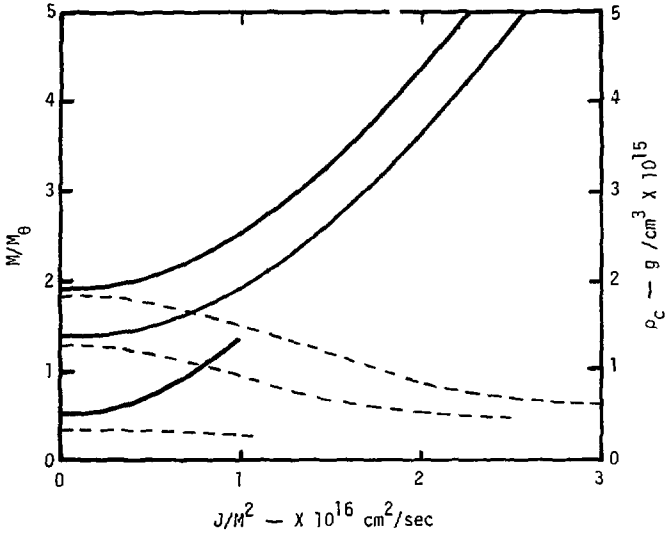

Wilson - Fig. 9

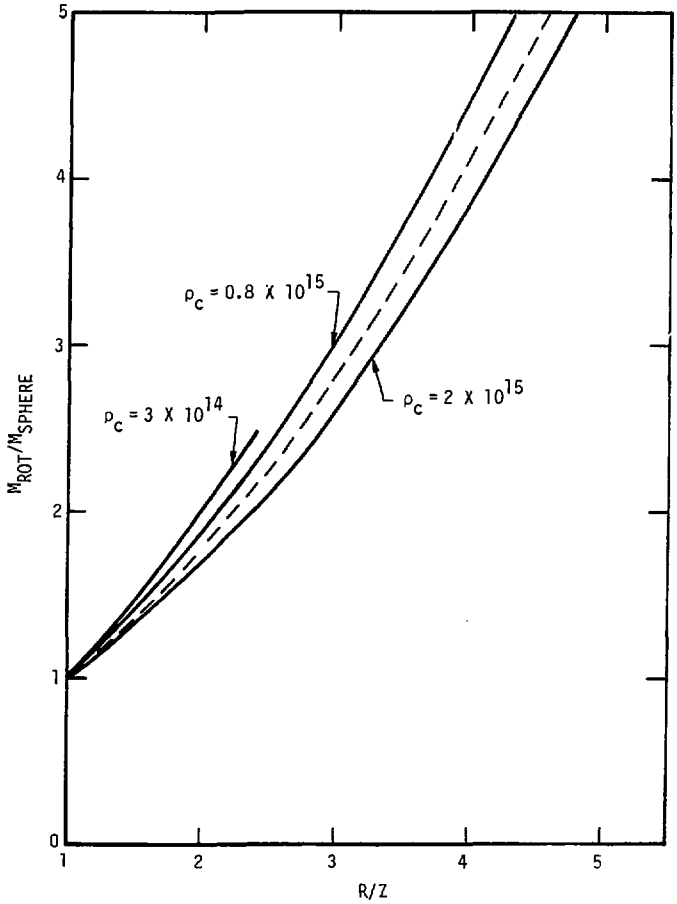

Wilson - Fig. 10.

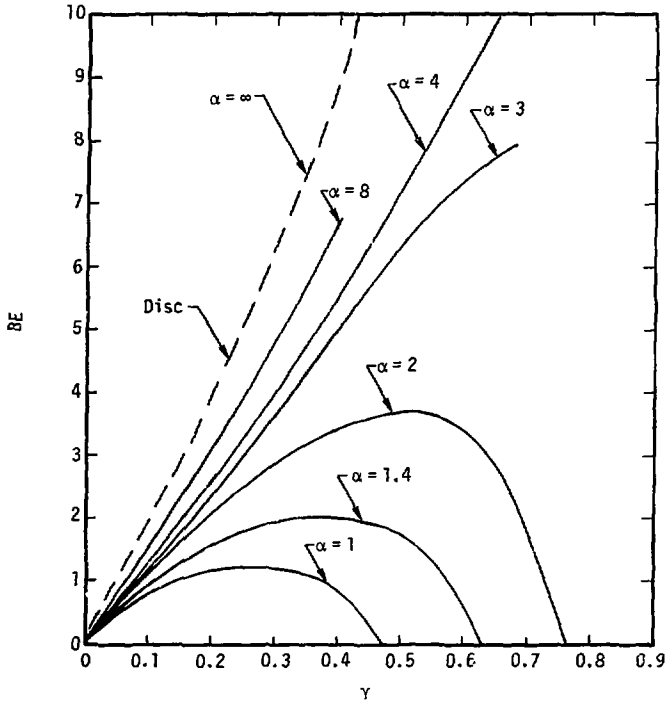

Wilson - Fig. 11.

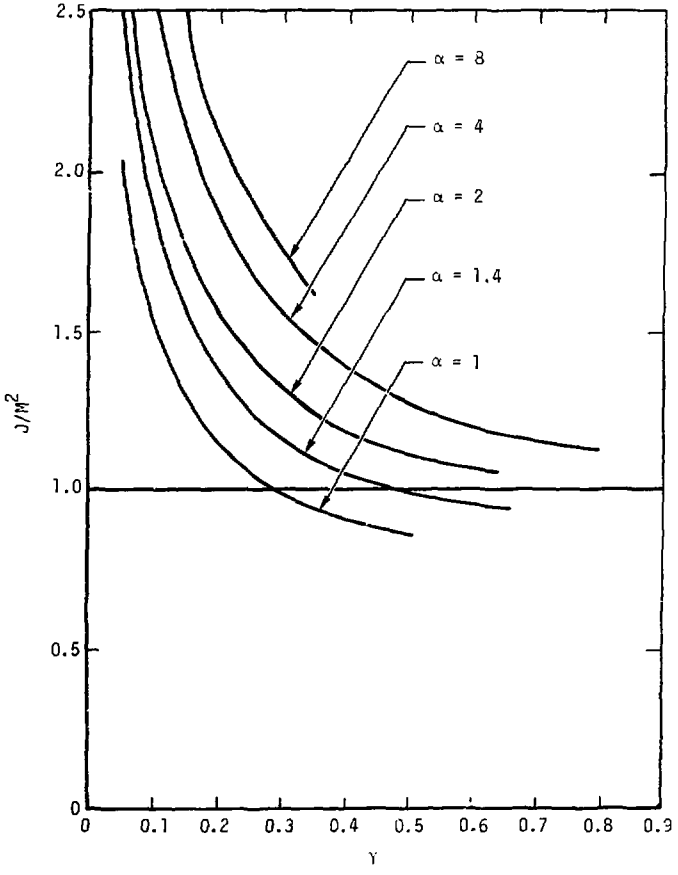

Wilson - Fig. 12

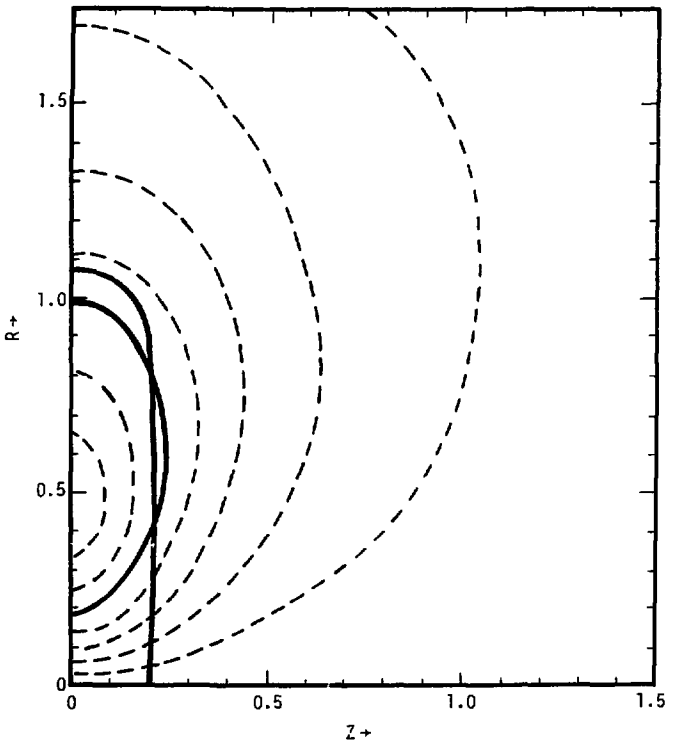

Wilson - Fig. 13

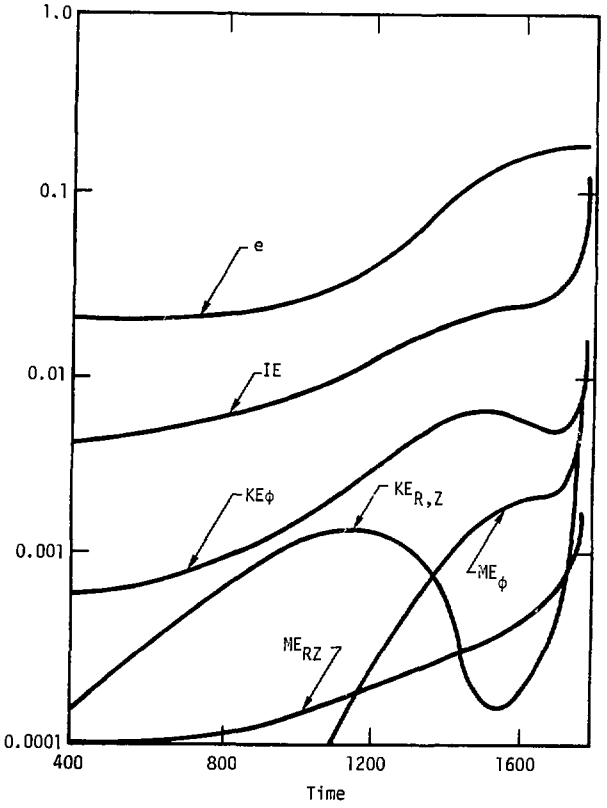

Wilson - Fig. 14

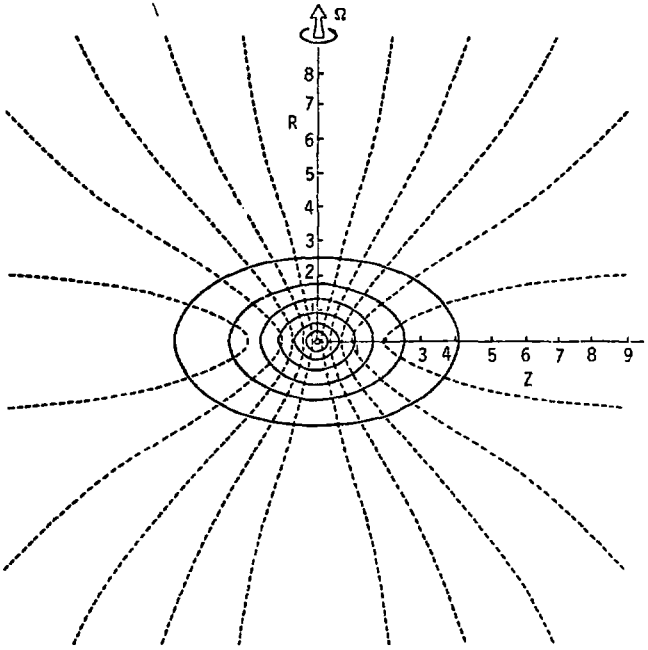

Wilson - Fig. 15

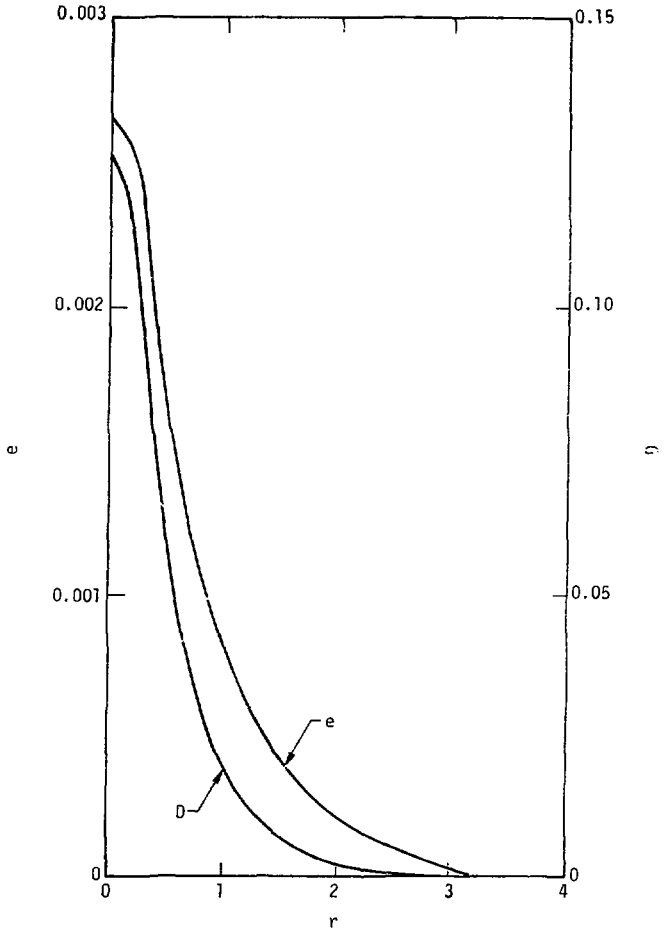

Wilson - Fig. 16

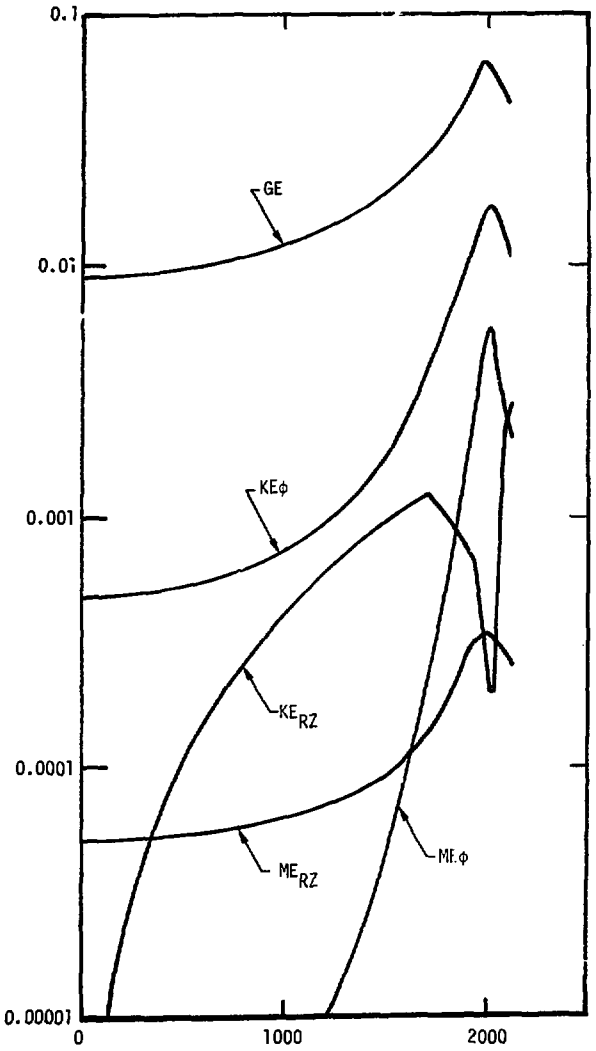

Wilson - Fig. 17

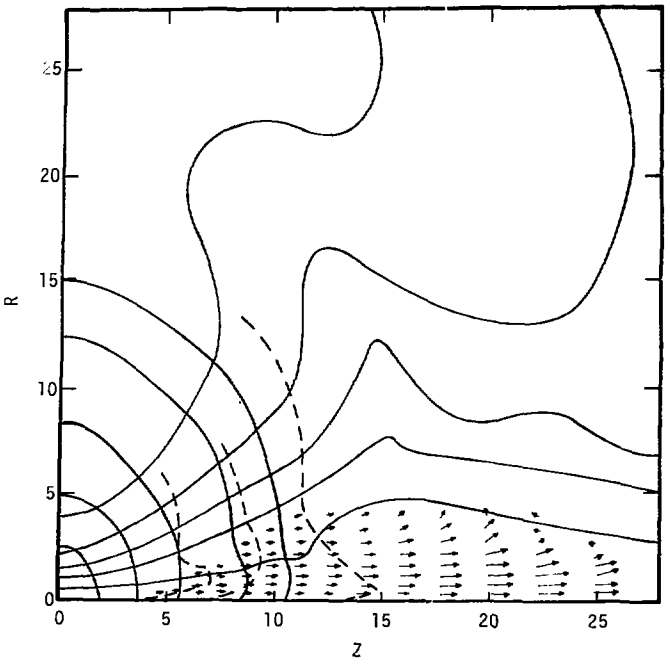

Wilson - Fig. 18

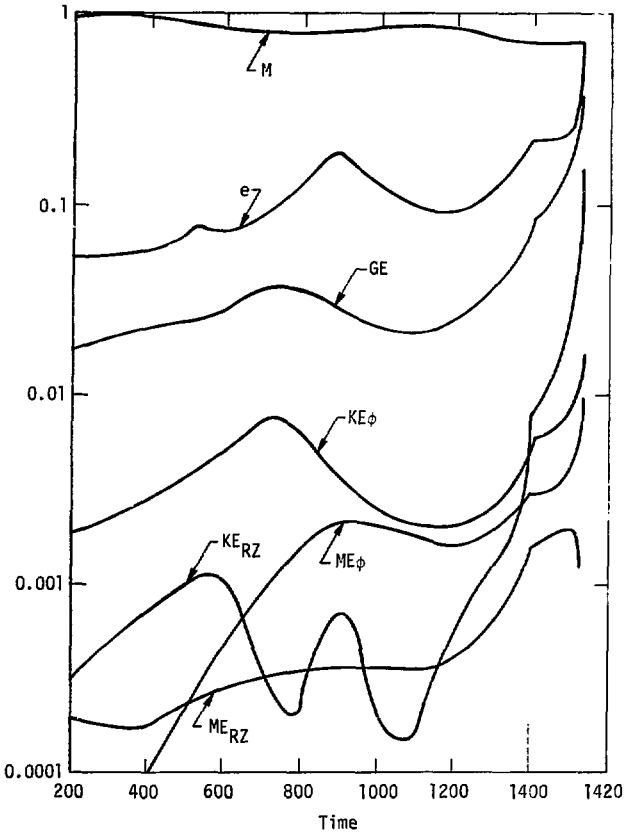

Wilson - Fig. 19

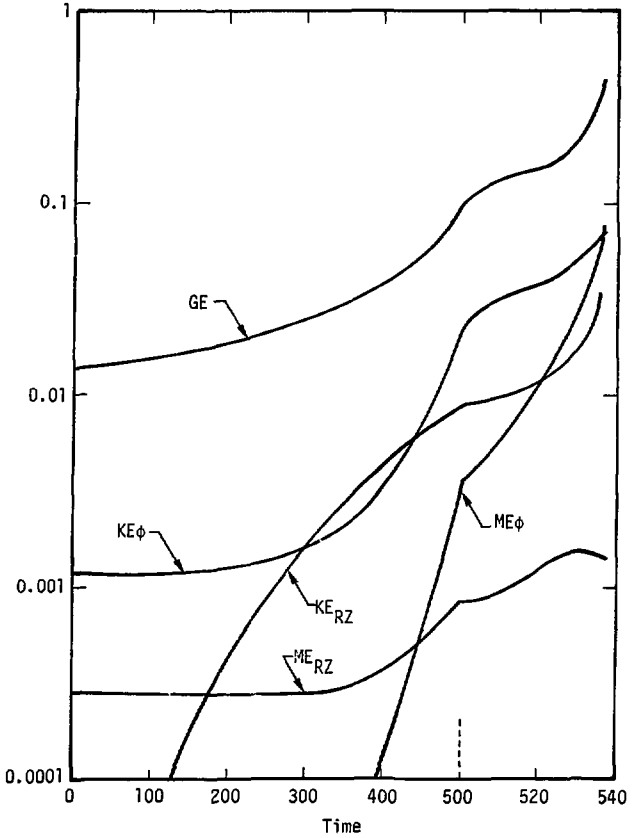

Wilson - Fig. 20

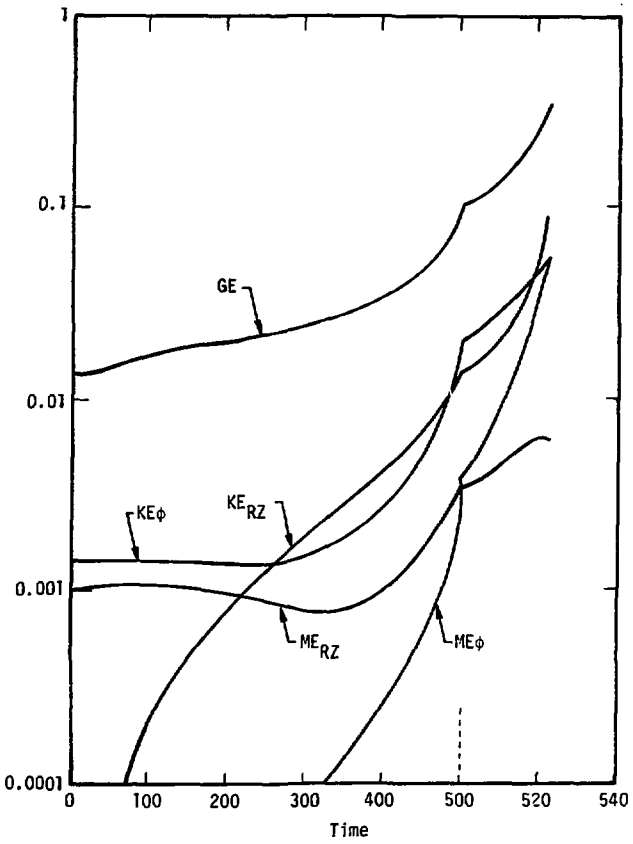

Wilson - Fig. 21

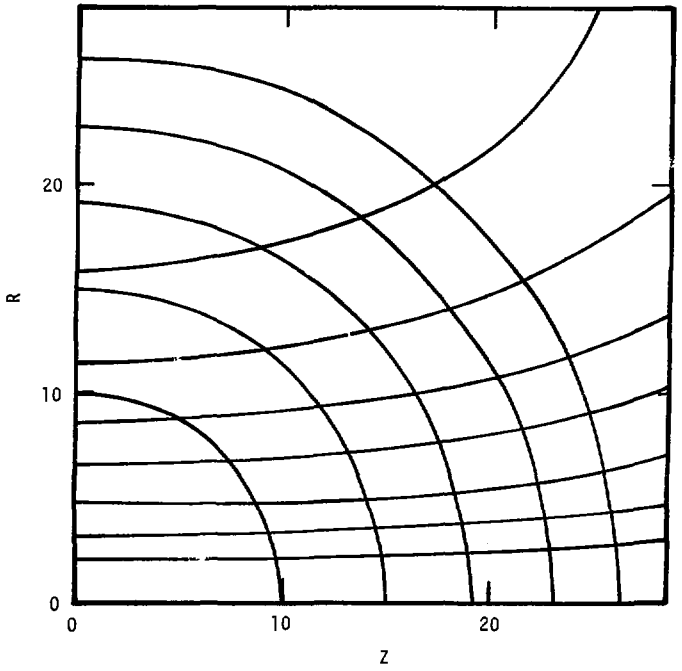

Wilson - Fig. 22

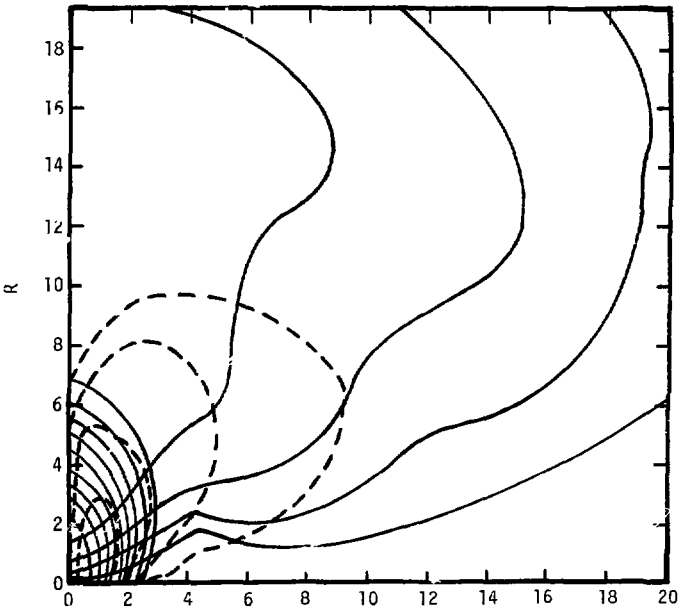

Wilson - Fig. 23

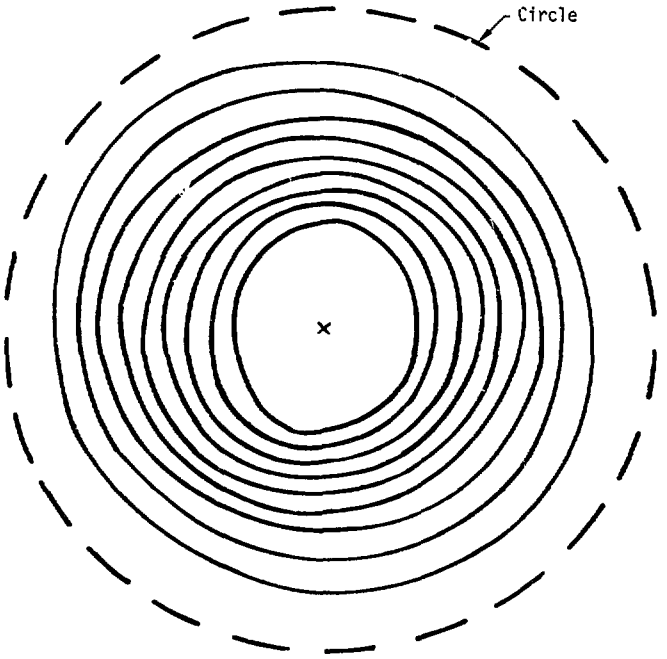

Wilson - Fig. 24

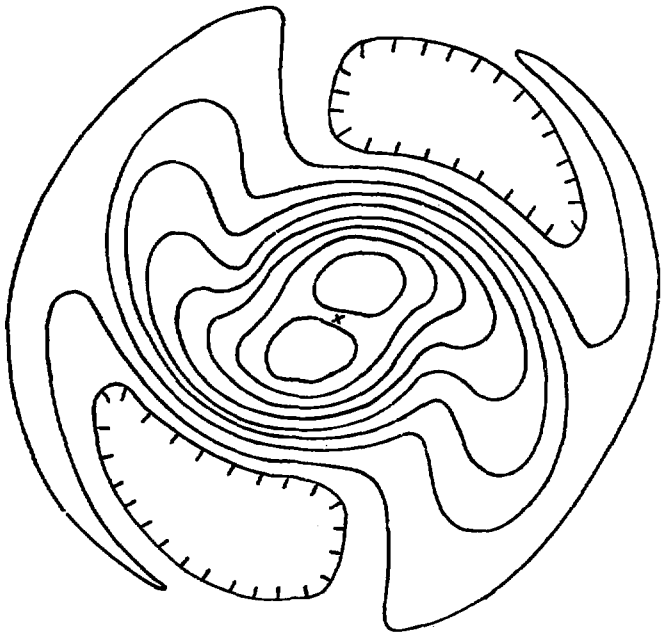

Wilson - Fig. 25